On the Analysis of Spatial Bandwidth in Double-Sided Near-Field Extremely Large-Scale MIMO Systems

Yijin Pan, Member, IEEE, Zhen Wang, Student Member, IEEE, Jun-Bo Wang, Senior Member, IEEE, Yijian Chen, Hongkang Yu, Jiangzhou Wang, Fellow, IEEE, and Kai-Kit Wong, Fellow, IEEE.

Abstract—This paper investigates the spatial bandwidth of line-of-sight (LoS) channels in extra-large MIMO (XL-MIMO) systems. For linear large-scale antenna arrays (LSAAs) with transceivers randomly positioned in 3D space, a simple but accurate closed-form expression is derived to characterize the local spatial bandwidth. Based on this analysis, we examine the properties of local spatial bandwidth and further derive expressions for the effective spatial bandwidth and the achievable degrees of freedom (i.e., the K number) for LSAAs. We also conduct case studies for both coplanar and non-coplanar transmitting and receiving arrays, providing more concise and intuitive expressions for local spatial bandwidth and achievable spatial degrees of freedom. Finally, the impact of array geometry on LoS XL-MIMO channel capacity is explored. When the transmitting and receiving arrays are coplanar and perpendicular to the line connecting their centers, the effective degree of freedom of the LoS channel is found to be approximately maximized. This orientation also maximizes the channel capacity in nearfield high-SNR scenarios.

Index Terms—Extra-large MIMO, large-scale antenna arrays, spatial bandwidth, degree of freedom, channel capacity.

I. INTRODUCTION

To meet the anticipated demands of future 6G networks in terms of data rates, connection density, latency, reliability, and coverage, array-based communication technologies have exhibited two significant trends: the adoption of large-scale antenna arrays (LSAA) and the use of higher carrier frequencies [1], [2]. The key characteristics of LSAA include not only an increased number of antennas but also an expanded

This work was supported in part by the National Natural Science Foundation of China under Grant No. 62371123, 62350710796 and 62331024, in part by ZTE Industry-University-Institute Cooperation Funds under Grant No.IA20240723011-PO0006, in part by Research Fund of National Mobile Communications Research Laboratory Southeast University under Grant No. 2025A03, and in part by the Engineering and Physical Sciences Research Council (EPSRC) under Grant EP/W026813/1. (Corresponding authors: Yijin Pan and Jun-Bo Wang).

- Y. Pan, Z. Wang, and J.-B. Wang are with the National Mobile Communications Research Laboratory, Southeast University, Nanjing, China (email: {panyj, wzhen, jbwang}@seu.edu.cn).
- Y. Chen and H. Yu are with the Wireless Product Research and Development Institute, ZTE Corporation, Shenzhen, China (email:{chen.yijian, yu.hongkang}@zte.com.cn).
- J. Wang is with the National Mobile Communications Research Laboratory, Southeast University, and Purple Mountain Laboratories, Nanjing, Jiangsu, China (email:{j.z.wang}@seu.edu.cn).
- K.-K. Wong is with the Department of Electronic and Electrical Engineering, University College London, Torrington Place, WC1E 7JE, UK, and also with Yonsei Frontier Lab, Yonsei University, Seoul, Korea. (email: kai-kit.wong@ucl.ac.uk).

array aperture, enabling LSAA communication systems to capture richer spatial domain information [3]. The high carrier frequency offers abundant bandwidth resources; however, due to higher penetration losses, multipath propagation is considerably weakened, which makes line-of-sight (LoS) array communication increasingly important [4]–[6].

The conventional view holds that LoS environments are unfavorable for multiple-input multiple-output (MIMO) communication, as MIMO channels in such scenarios cannot provide spatial multiplexing gains [7]. However, in extralarge MIMO (XL-MIMO) systems, the use of LSAA may position users predominantly within the near-field radiation of access points, which challenges the traditional assumption of plane-wave propagation. Instead, a more general non-uniform spherical wave propagation model is required to accurately characterize phase and amplitude variations within the array [8], [9]. Within the near-field region, spherical waves exhibit nonlinear changes in phase and power levels across each link. thereby increasing the rank of the channel matrix [10]. This significantly enhances the spatial degrees of freedom (DoF) in MIMO channels within near-field environments, even under LoS conditions, making spatial multiplexing feasible for LoS XL-MIMO systems.

The analysis of spatial DoF provides insights into the number of independent signal dimensions available for transmitting information over wireless channels [10]. The spatial DoF is influenced by various factors, such as the geometric configuration of the antenna arrays, the propagation environment, and the polarization of the antennas. It is important to note that, while DoF quantifies the number of independent parallel sub-channels, it does not account for the actual gain of each sub-channel. In practice, only sub-channels that achieve sufficient power levels are considered effective. The gains of these effective sub-channels can be represented by the singular values of the channel matrix, and the effective degrees of freedom (EDoF) correspond to the DoF that are exploitable.

Significant progress has been made in understanding EDoF by current researchers. In [11], the authors approximate EDoF using the expression $\mathsf{EDoF}_1 = (\mathsf{tr}\left(\mathbf{H}\mathbf{H}^H\right)/\|\mathbf{H}\mathbf{H}^H\|_F)^2$. In [12], the EDoF of continuous-aperture (CAP) MIMO is explored through an exact eigendecomposition of the Hermitian kernel of the Green's function. [13] and [14] employed Landau's eigenvalue theorem to evaluate EDoF. These studies demonstrated that EDoF can be enhanced by reducing the propagation distance or increasing the aperture size. In fact,

1

for the LoS environments, the channel characteristics are determined by the geometric properties of the transmitting and receiving arrays, including their size, position, and orientation. However, the impact of array geometry on EDoF has not been highlighted in these studies.

In [15] and [16], the authors investigated the EDoF of near-field CAP-MIMO using the Nyquist sampling theorem and Fourier theory. Building on this, researchers proposed an approximation method to calculate the EDoF between two CAP arrays, treating the EDoF as the number of Nyquist rate samples required to represent a 2D band-limited signal [1]. In [17], closed-form approximations for each orthogonal receiving direction were derived through an orthogonal decomposition of the receiving directions, and the impact of array position and rotation on achievable spatial DoF was analyzed. Additionally, [18] employed a dual-slope asymptotic expression to approximate the spatial bandwidth at the center of the receiving array and used this expression to analyze the channel's DoF performance.

Although [18] provided approximate expressions for spatial bandwidth, its derivation relies on complex piecewise function fitting, which overlooks the intuitive geometric insights. In [19], the impact of the array geometry on the number of distinguishable spatial frequency bins and the spatial DoF has been shown to be highly related. However, some interesting properties of spatial bandwidth remain unexplored. Additionally, the impact of adjusting array geometry to increase nearfield channel capacity has not been discussed. To address these issues, this paper derives a simple yet accurate closedform expression for the local spatial bandwidth of LSAA. The obtained result highlights the impacts of the aperture sizes of the transceiver arrays, as well as their relative position and orientation, on the local spatial bandwidth. These properties can be effectively transferred to analyze the effective spatial bandwidth of the array, the EDoF of the channel, and the channel capacity.

The main contributions of this paper are summarized as follows:

- For arbitrary placement of the transceiver arrays in 3D space, we derive an interpretable closed-form expression for the local spatial bandwidth at the center of the receiving array. Then, we further analyze the maximum and expectation of the local spatial bandwidth.
- Closed-form expressions for the effective spatial bandwidth of the receiving array, along with numerical and approximate closed-form expressions for the achievable degrees of freedom (i.e., the K number), are also provided. We thoroughly investigate the relationship between the effective spatial bandwidth, the K number, and the local spatial bandwidth. Additionally, we validate the correlation between the K number and the EDoF. Through case studies of coplanar and non-coplanar transceiver arrays, we present more concise and intuitive results for the local spatial bandwidth and the K number.
- With the derived the K number, we further explore the impact of array geometry on the capacity of LoS XL-MIMO channels. Our results demonstrate that the geometric configuration of the array has a negligible impact

on channel capacity even in the far-field communications. However, in the near field, adjusting the array geometry can manipulate the distribution of the channel's singular values, thereby achieving optimal channel capacity at different receiving signal-to-noise (SNR).

The remainder of this paper is organized as follows: Section II introduces the problem settings and assumptions, derives the closed-form expression and the related properties for local spatial bandwidth. In Section III, we examine the effective spatial bandwidth, the K number, and demonstrate the correlation between the K number and EDoF. Also, we conduct case studies for both coplanar and non-coplanar arrays, offering more concise results for local spatial bandwidth and the K number. Section IV explores the impact of array geometry on LoS XL-MIMO channel capacity, and finally, Section V concludes the paper. Part of this paper was presented at the IEEE WCSP 2024 [20]. The journal version provides a more comprehensive analysis of spatial bandwidth and further investigates the impact of array geometry on channel capacity.

Notations: lower-case, bold-case, and bold upper-case letters represent scalars, vectors, and matrices, respectively; $[\cdot]^*$, $[\cdot]^T$, and $[\cdot]^H$ denote the conjugate, transpose, and conjugate-transpose operations, respectively; \mathbf{I}_N denotes an $N \times N$ identity matrix; $\operatorname{Re}\{\cdot\}$ denotes the real part of the argument; $\mathcal{CN}(\boldsymbol{\mu}, \boldsymbol{\Sigma})$ denotes the complex multivariate Gaussian distribution with mean $\boldsymbol{\mu}$ and variance $\boldsymbol{\Sigma}$.

II. LOCAL SPATIAL BANDWIDTH ANALYSIS

This section presents the foundation of local spatial bandwidth and analyzes the impact of array position and orientation on local spatial bandwidth. The analytical approach is provided to clarify the impact of array geometry, including the array position and the orientation, on the effective spatial bandwidth and the EDoF of the channel.

A. Problem Settings and Assumptions

As shown in Fig.1, we consider an XL-MIMO system where both the transmitter and receiver are equipped with LSAA arrays, denoted by \mathcal{L}_s and \mathcal{L}_p , with respective dimensions L_s and L_p . The transmitting array \mathcal{L}_s is centered at the origin O and oriented along the z-axis. The point P represents the center of the receiving array \mathcal{L}_p , with coordinates $\mathbf{p}_0 = [x_p, y_p, z_p]^{\mathrm{T}}$. The orientation of the \mathcal{L}_p is given by the unit vector $\hat{\mathbf{v}} = [v_x, v_y, v_z]^{\mathrm{T}}$, where $v_z \geq 0$ and $\|\hat{\mathbf{v}}\| = 1$. Under the assumption of an ideal isotropic point source, rotating \mathcal{L}_p around the z-axis does not affect its observed electric field.

Due to limited diffraction and high absorption, mmWave signals exhibit weak multipath propagation, making the LoS component dominant [21], [22]. Accordingly, we consider the LoS wireless channel under 3D free-space propagation conditions. Under the assumption of a time-harmonic current distribution¹ on \mathcal{L}_s , the electric field perceived by position $p \in \mathcal{L}_p$ can be expressed as [23]:

$$\mathcal{E}(p) = \int_{\mathcal{L}_s} \mathcal{G}(p-s) \mathcal{J}(s) ds,$$
 (1)

¹We focus on a narrowband channel, as the same approach can be readily extended to analyze each subcarrier in a wideband system.

where $\mathcal{J}(s)$ represents the current density at point $s \in \mathcal{L}_s$. $\mathcal{G}(p-s)$ represents the Green's function (e.g., the spatial impulse response [23]). In this case, the Green's function² can be expressed as [18], [24]:

$$\mathbf{\mathcal{G}}(\mathbf{r}) \triangleq \frac{j\omega\mu}{4\pi r} \exp\left(-jk_0 r\right) \left(\mathbf{I} - \hat{\mathbf{r}}^{\mathrm{T}} \hat{\mathbf{r}}\right), \tag{2}$$

where $r \triangleq p-s$ denotes the propagation vector, $r = \|r\|$ is the propagation distance, and $\hat{r} = r/\|r\|$ is the unit vector in the direction of propagation. ω denotes the (angular) frequency of the waves, and $k_0 = \omega \sqrt{\epsilon \mu} = \frac{2\pi}{\lambda}$ denotes the wavenumber, where ϵ and μ represent the permittivity and permeability of free space, respectively.

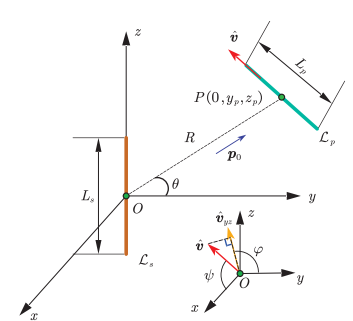


Fig. 1: System model.

Definition 1. The *spatial frequency*³ of the wave component $\mathcal{G}(r) \mathcal{J}(s) ds$ generated by the source $s \in \mathcal{L}_s$, measured at $p \in \mathcal{L}_p$, as it moves along \hat{v} , is given by

$$f_{\hat{\boldsymbol{v}}}(\boldsymbol{p}, \boldsymbol{s}) = k_0 \hat{\boldsymbol{r}}^{\mathrm{T}}(\boldsymbol{p}, \boldsymbol{s}) \hat{\boldsymbol{v}},$$
 (3)

where vector $\hat{r}(\boldsymbol{p},s) = (\boldsymbol{p}-s)/\|\boldsymbol{p}-s\|$ denotes the propagation direction, as depicted in Fig. 2. From (3), it is evident that the spatial frequency $f_{\hat{v}}(\boldsymbol{p},s)$ can be expressed as the inner product of the propagation unit vector and receiving array direction unit vector. With the wavenumber, we have $-k_0 \leq f_{\hat{v}}(\boldsymbol{p},s) \leq k_0$.

B. Closed-Form Expression for Local Spatial Bandwidth

For simplicity, we derive the expression for the local spatial bandwidth at the center point of \mathcal{L}_p . Note that the local spatial bandwidth at any point in 3D space can be obtained using the same method.

As shown in Fig. 1, without loss of generality, it is assumed that the center point P of \mathcal{L}_p lies in the first quadrant of the yOz plane (including the boundary), i.e., $x_p = 0$, $y_p \ge 0$, and $z_p \ge 0$. R = |OP| denote the distance between \mathcal{L}_s and \mathcal{L}_p , and let θ be the angle between the vector \mathbf{p}_0 and the positive y-axis $\hat{\mathbf{y}} = [0, 1, 0]^T$. Therefore, the position of P is given by $\mathbf{p}_0 = [0, R\cos\theta, R\sin\theta]^T$.

It is clear that different locations $s' \in \mathcal{L}_s$ generate distinct spatial frequency components at p_0 . Accordingly, the *local spatial bandwidth* is defined as follows:

Definition 2. The *local spatial bandwidth*⁴ at p_0 is defined as the difference between the maximum and minimum spatial frequencies of all wave components radiated by \mathcal{L}_s at p_0 , given by

$$\omega_{\hat{\boldsymbol{v}}}\left(\boldsymbol{p}_{0}, \mathcal{L}_{s}\right) = k_{0} \left(\max_{\boldsymbol{s} \in \mathcal{L}_{s}} \hat{\boldsymbol{r}}^{\mathrm{T}}\left(\boldsymbol{p}_{0}, \boldsymbol{s}\right) \hat{\boldsymbol{v}} - \min_{\boldsymbol{s} \in \mathcal{L}_{s}} \hat{\boldsymbol{r}}^{\mathrm{T}}\left(\boldsymbol{p}_{0}, \boldsymbol{s}\right) \hat{\boldsymbol{v}} \right). \tag{4}$$

From (4), it is clear that $0 \leq \omega_{\hat{v}}(p_0, \mathcal{L}_s) \leq 2k_0$. Note that $\omega_{\hat{v}}(p_0, \mathcal{L}_s)$ depends on the position of the observation point p_0 and the orientation \hat{v} of \mathcal{L}_p . Unfortunately, there is no precise closed-form expression for the local bandwidth of transmitting and receiving arrays arbitrarily placed in 3D space.

To derive the closed-form expression for $\omega_{\hat{v}}$ (p_0, \mathcal{L}_s), the key idea is to characterize the relationship between the range of variation of the propagation direction vector \hat{r} and the position p_0 . To simplify the derivations, we introduce γ to represent the angle between \hat{r} (p_0, s) and the positive y-axis. Thus, the propagation direction vector \hat{r} can be expressed as

$$\hat{\boldsymbol{r}}(\boldsymbol{p}_0, \boldsymbol{s}) \triangleq \hat{\boldsymbol{r}}(\gamma) = [0, \cos \gamma, \sin \gamma]^{\mathrm{T}},$$
 (5)

Since A, P, and B are situated in the yOz plane, the x-axis component of \hat{r} is zero. Therefore, to describe the range of variation of the propagation direction vector \hat{r} , we only need to determine the range of variation of γ as s moves along \mathcal{L}_s .

As shown in Fig. 2, let $\alpha = \angle APB$ represent the angle subtended by P with respect to A and B, satisfying $0 < \alpha < \pi$. Construct the circumcircle of triangle APB, intersecting the y-axis at points M and N, with O' as its center. Connect MP, noting that MP serves as the bisector of solid angle α . S is the intersection of MP and the z-axis. Let $\beta = \angle PMN$, with $0 \le \beta \le \pi/2$. Thus, the range of γ can be determined by the angle tuple (α, β) :

$$-\alpha/2 + \beta \le \gamma \le \alpha/2 + \beta. \tag{6}$$

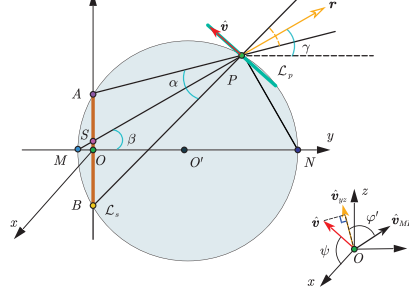


Fig. 2: The range of variation of the propagation direction vector \hat{r} .

Similarly, we express the orientation $\hat{\boldsymbol{v}}$ of \mathcal{L}_p using a pair of angles (ψ, φ) :

$$\hat{\boldsymbol{v}}(\psi,\varphi) = \left[\cos\psi, \sin\psi\cos\varphi, \sin\psi\sin\varphi\right]^{\mathrm{T}}, \tag{7}$$

where ψ denotes the elevation angle of \hat{v} with respect to the positive x-axis, satisfying $0 \le \psi \le \pi$. \hat{v}_{yz} is the projection

²The analysis is restricted to the radiating near-field and far-field regions, where the distance between \mathcal{L}_p and \mathcal{L}_s exceeds 10 times the electromagnetic wavelength λ .

³More detailed discussions of spatial frequency can be found in [19].

⁴When the receive array is a two-dimensional surface, the local spatial bandwidth is determined by the area of the region spanned by the projection of \hat{r} [1].

of \hat{v} onto the yOz plane. The angle φ represents the azimuth angle, which is defined as the angle between \hat{v}_{yz} and the y-axis, with $0 \le \varphi \le \pi$.

Based on (5) and (7), the spatial frequency $f_{\hat{v}}(p_0, s)$ can be reformulated using angle tuple (ψ, φ, γ) as:

$$f_{\hat{\boldsymbol{v}}}(\boldsymbol{p}_0, \boldsymbol{s}) \triangleq f(\psi, \varphi, \gamma) = k_0 \hat{\boldsymbol{r}}^{\mathrm{T}}(\gamma) \hat{\boldsymbol{v}}(\psi, \varphi)$$

= $k_0 \sin \psi \cos(\gamma - \varphi).$ (8)

From (8), each position s along \mathcal{L}_s results in the reception of wave components with different spatial frequencies at point P. Let $F^{\max}\left(\psi,\varphi;\alpha,\beta\right)$ and $F^{\min}\left(\psi,\varphi;\alpha,\beta\right)$ denote the maximum and minimum values of the spatial frequency received at point P when \mathcal{L}_p is oriented as $\hat{v}\left(\psi,\varphi\right)$, respectively, as follows:

$$F^{\max}(\psi, \varphi; \alpha, \beta) \triangleq \max_{-\alpha/2 + \beta \le \gamma \le \alpha/2 + \beta} f(\psi, \varphi, \gamma), \quad (9)$$

$$F^{\min}\left(\psi,\varphi;\alpha,\beta\right) \triangleq \min_{-\alpha/2+\beta \le \gamma \le \alpha/2+\beta} f\left(\psi,\varphi,\gamma\right). \tag{10}$$

According to (4), the local spatial bandwidth received at p_0 can be expressed as

$$\omega_L(\psi, \varphi; \alpha, \beta) = F^{\max}(\psi, \varphi; \alpha, \beta) - F^{\min}(\psi, \varphi; \alpha, \beta).$$
(11)

It can be verified that for any (α, β) , we have

$$\omega_L(\psi, \varphi; \alpha, \beta) = \omega_L(\psi, \varphi + \pi; \alpha, \beta). \tag{12}$$

This implies that it is sufficient to examine the function $\omega_L(\psi,\varphi;\alpha,\beta)$ over any interval of length π for φ . Without loss of generality, we can consider the case where $\varphi \in [\beta,\beta+\pi]$. As shown in Fig. 3, define $\varphi' \triangleq \varphi - \beta$, which represents the angle of \hat{v}_{yz} relative to \hat{v}_{MP} , where $\hat{v}_{MP} = \overrightarrow{MP} / |\overrightarrow{MP}|$. Then, for $\omega_L(\psi,\varphi';\alpha,\beta)$ over $\psi \in [0,\pi]$ and $\varphi' \in [0,\pi]$, substituting (8) into (9), (10), we have

$$F^{\max}(\psi, \varphi'; \alpha, \beta) = \begin{cases} k_0 \sin \psi, \varphi' \in [0, \alpha/2], \\ k_0 \sin \psi \cos (\alpha/2 - \varphi'), \varphi' \in (\alpha/2, \pi], \end{cases}$$
(13)

and

$$F^{\min}(\psi, \varphi'; \alpha, \beta) = \begin{cases} k_0 \sin \psi \cos (-\alpha/2 - \varphi'), \varphi' \in [0, \pi - \alpha/2), \\ -k_0 \sin \psi, \varphi' \in [\pi - \alpha/2, \pi]. \end{cases}$$
(14)

According to (11), (13), and (14), we obtain the following expression for the local spatial bandwidth at p_0 :

$$\omega_{L}(\psi, \varphi'; \alpha, \beta) = \begin{cases} k_{0} \sin \psi \left[1 - \cos\left(-\alpha/2 - \varphi'\right)\right], 0 \leq \varphi' \leq \alpha/2, \\ 2k_{0} \sin \psi \sin(\alpha/2) \sin \varphi', \alpha/2 < \varphi' < \pi - \alpha/2, \\ k_{0} \sin \psi \left[1 + \cos\left(\alpha/2 - \varphi'\right)\right], \pi - \alpha/2 \leq \varphi' \leq \pi. \end{cases}$$

$$(15)$$

Remark 1: It is noteworthy that, unlike the approximate expressions derived in [17] and [18], we provide an accurate formulation of the local spatial bandwidth in (15) without the need for complex approximations and fitting techniques. Based on the definition of local spatial bandwidth in (4), it is evident that the local spatial bandwidth at point P depends solely on the relative geometric configuration between

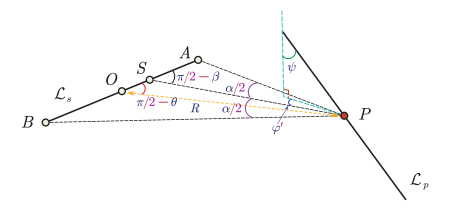


Fig. 3: The relative geometric relationship between the transmitting and receiving arrays.

the receiving and transmitting arrays. As the receiving array rotates around the z-axis, this relative geometric relationship remains unchanged, thereby keeping the local spatial bandwidth at point P unchanged. Consequently, for any point in the 3D space, we can rotate it around the z-axis to align it with the yOz-plane, and then use (15) to determine its local spatial bandwidth. Moreover, (15) provided an intuitive geometric interpretation of the factors influencing local spatial bandwidth. Specifically, the expression is characterized by two sets of angle parameters: the first set (ψ, φ') relates to the orientation \hat{v} of \mathcal{L}_p , and the second set (α, β) relates to the position p_0 of \mathcal{L}_p . Additionally, it is observed that in (15), ψ and φ' are decoupled, allowing us to independently study the impacts of the elevation angle and the azimuth angle on the received spatial bandwidth. This expression enables the fast and accurate determination of spatial bandwidth at various points in space, thereby accelerating system-level simulations.

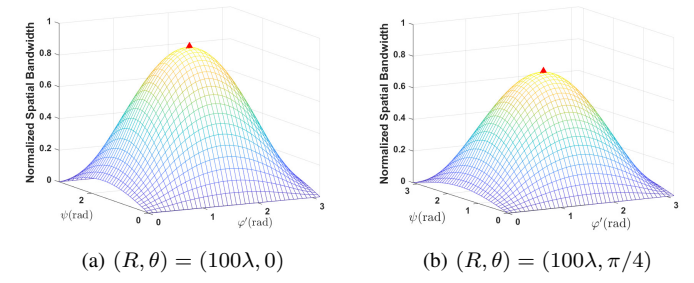


Fig. 4: The normalized local spatial bandwidth observed at different the receiving orientations (ψ, φ') .

Fig. 4 plots the normalized local spatial bandwidth ω_L/k_0 as a function of the orientation (ψ,φ') of the receiving array, based on (15). The dimension of the transmitting array is $L_s=100\lambda$, and the position of P is described by (R,θ) . The red triangle in the figure marks the receiving orientation that maximizes the local spatial bandwidth.

From Fig. 4a, it is observed that the local spatial bandwidth ω_L at P initially increases and then decreases as ψ varies from 0 to π . For all $\varphi' \in [0,\pi]$, ω_L reaches its maximum value when $\psi = \pi/2$. Notably, at this point, the component of \hat{v} along positive x-axis is zero, indicating that \mathcal{L}_p and \mathcal{L}_s are coplanar. When ψ is either 0 or π , i.e., when \mathcal{L}_p is perpendicular to \mathcal{L}_s , ω_L attains its minimum value of zero. Similarly, as φ' changes from 0 to π , the local spatial bandwidth ω_L at P also increases initially and then decreases. For all $\psi \in [0,\pi]$, ω_L achieves its maximum value when $\varphi' = \pi/2$. The maximum value of ω_L is attained when $(\psi,\varphi') = (\pi/2,\pi/2)$. As shown in Fig. 4b, the trend of ω_L remains consistent with that observed in Fig. 4a, which is due to the use of relative orientation angles (ψ,φ') to describe the orientation of the \mathcal{L}_p . Moreover, the maximum

value of ω_L is smaller than that in the case of $\theta = 0$, as the corresponding value of α is reduced in this configuration.

Fig. 5 compares the normalized local bandwidth obtained by different approaches. "PROP" represents the results obtained using (15), "NUME" refers to the numerical calculation results using the definition (4), and "DSAF" corresponds to the results computed using the dual-slope asymptotic function proposed in [18].

Comparing Fig. 5a and Fig. 5b, we observe that when the transceiver distance R is large, all three methods yield nearly identical results. However, when R is small, the proposed approach of local spatial bandwidth perfectly matches the numerical results, while the "DSAF" method exhibits larger errors. Furthermore, when $\varphi'=0$, the local spatial bandwidth obtained by the "DSAF" method is zero, which is contradicted by the numerical calculation results.

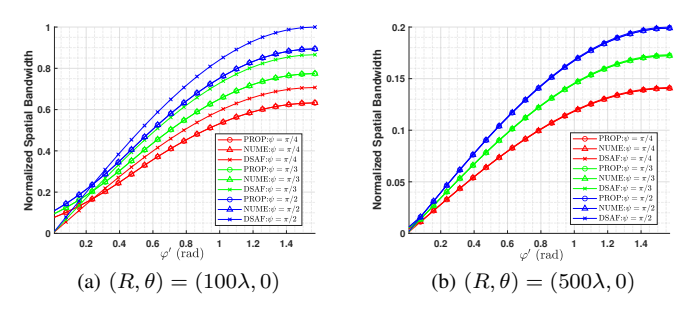


Fig. 5: The calculation results of the normalized local spatial bandwidth under different schemes.

C. Maximum and Expectation of the Local Spatial Bandwidth

Using (15), we can further explore the relationship between the local spatial bandwidth and the received position parameters (α, β) of \mathcal{L}_p . First, we investigate the maximum value of the local spatial bandwidth at a given location, defined as

$$\omega_L^{\max}(\alpha, \beta) = \max_{\psi, \varphi} \ \omega_L(\psi, \varphi; \alpha, \beta). \tag{16}$$

Proposition 1: For any point P in 3D space, the local spatial bandwidth ω_L at P reaches its maximum value if and only if the receiving direction $\hat{\boldsymbol{v}}$ satisfies $\hat{\boldsymbol{v}} = \pm \hat{\boldsymbol{v}}_{NP}$, where $\hat{\boldsymbol{v}}_{NP} = \overrightarrow{NP}/|\overrightarrow{NP}|$. The maximum value $\omega_L^{\max}(\alpha,\beta)$ is given by

$$\omega_L^{\max}(\alpha, \beta) = 2k_0 \sin(\alpha/2). \tag{17}$$

Proof: Since (15) is a piecewise function, ω_L^{max} is determined by the maximum value of each segment. According to (12),

$$\omega_L^{\max} = \max_{\psi \in [0,\pi], \varphi' \in [0,\pi]} \ \omega \left(\psi, \varphi'; \alpha, \beta \right). \tag{18}$$

When $0 \le \varphi' \le \alpha/2$, we have

$$\omega_L(\psi, \varphi') \le k_0 (1 - \cos \alpha), \tag{19}$$

the equality is attained when $(\psi, \varphi') = (\pi/2, \alpha/2)$. When $\alpha/2 \le \varphi' \le \pi - \alpha/2$, we have

$$\omega_L(\psi, \varphi') \le 2k_0 \sin(\alpha/2),$$
 (20)

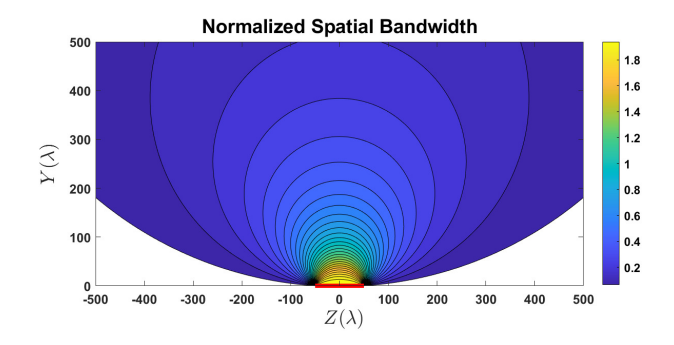


Fig. 6: Maximum normalized local spatial bandwidth at different observation locations.

the equality is attained when $(\psi, \varphi') = (\pi/2, \pi/2)$. When $\pi - \alpha/2 \le \varphi' \le \pi$, we have

$$\omega_L(\psi, \varphi') \le k_0 (1 - \cos \alpha),$$
 (21)

the equality is attained when $(\psi, \varphi') = (\pi/2, \pi - \alpha/2)$. Thus,

$$\omega_L^{\text{max}} = k_0 \cdot \max\left\{1 - \cos\alpha, 2\sin\left(\alpha/2\right)\right\} = 2k_0\sin\left(\alpha/2\right). \tag{22}$$

Note that at this point, $\hat{\boldsymbol{v}} = \hat{\boldsymbol{v}}_{NP}$.

Remark 2: According to Proposition 1, the maximum local spatial bandwidth ω_L^{\max} at P depends solely on the solid angle α subtended by P and the two ends of \mathcal{L}_s . With $\alpha \in (0,\pi)$, the maximum local spatial bandwidth increases with α , which increases with the transmitting array aperture. The orientation \hat{v} that corresponds to this maximum value ω_L^{\max} , however, depends on the angle β . Furthermore, based on geometric relationships, any point P' on the circular arc \widehat{APB} has the same maximum local spatial bandwidth ω_L^{\max} .

Fig. 6 illustrates the maximum normalized local spatial bandwidth for different locations in the yOz-plane when $L_s=100\lambda$. The y- and z-axes are normalized by the wavelength λ . The red line along the z-axis indicates the position of the transmit array \mathcal{L}_s . The black lines represent contour lines, along which the maximum value of local spatial bandwidth is identical at each location. For a fixed observation angle θ , ω_L^{\max} decreases as R increases, and the decreasing rate of ω_L^{\max} slows down with increasing R. When R is fixed and $R > L_s/2$, ω_L^{\max} increases as θ approaches 0. Additionally, it is observed that the contour lines of ω_L^{\max} form circles with \mathcal{L}_s as their chord. Building on the concept of effective aperture, the proposed method for analyzing the maximum local spatial bandwidth can also be extended to other types of arrays, such as planar arrays and circular arrays [25].

When the orientation of \mathcal{L}_p is unknown and arbitrary, the expected value of the spatial bandwidth received at \mathcal{L}_p 's center point P depends on its position. As demonstrated later, the expected value of the local spatial bandwidth on the receiving array is related to the expected value of the EDoF of the channel. Without loss of generality, \mathcal{L}_p has the isotropic distribution in 3D space of the direction \hat{v} , i.e., the orientation vector \hat{v} is equally likely to point to any direction, then the joint probability density function (PDF) for (ψ, φ') is given by

$$p_{\psi,\varphi'}^{3D}(\psi,\varphi') = p_{\psi}(\psi) p_{\varphi'}(\varphi'), \qquad (23)$$

where $p_{\psi}(\psi) = 0.5\sin\psi$ for $\psi \in [0,\pi]$ and $p_{\varphi'}(\varphi') = 1/(2\pi)$ for $\varphi' \in [0,2\pi]$ are the PDFs of ψ and φ' , respectively. Consequently, the expectation of the local spatial bandwidth at point P is given by

$$\mathbb{E}_{p_{\psi,\varphi'}^{3D}} \left\{ \omega_L \left(\psi, \varphi'; \alpha, \beta \right) \right\}$$

$$= \int_0^{\pi} \int_0^{2\pi} \omega_L \left(\psi, \varphi'; \alpha, \beta \right) p_{\psi,\varphi'}^{3D} \left(\psi, \varphi' \right) d\psi d\varphi' \qquad (24)$$

$$= \frac{k_0}{4} \left(\alpha + 2 \sin \frac{\alpha}{2} \right).$$

When \mathcal{L}_p is constrained to be coplanar with that of \mathcal{L}_s , we have $\psi = \pi/2$. Consequently, the joint PDF for (ψ, φ') is given by

$$p_{\psi,\varphi'}^{\text{2D}}(\psi,\varphi) = \delta(\psi - \pi/2) p_{\varphi'}(\varphi'), \qquad (25)$$

where $\delta(\cdot)$ represents the Dirac delta function. The expectation of the local spatial bandwidth at point P under these conditions is then given by

$$\mathbb{E}_{p_{\psi,\varphi'}^{2D}} \left\{ \omega_L \left(\psi, \varphi'; \alpha, \beta \right) \right\}$$

$$= \int_0^{\pi} \int_0^{2\pi} \omega_L \left(\psi, \varphi'; \alpha, \beta \right) p_{\psi,\varphi'}^{2D} \left(\psi, \varphi' \right) d\psi d\varphi' \qquad (26)$$

$$= \frac{k_0}{\pi} \left(\alpha + 2 \sin \frac{\alpha}{2} \right).$$

Comparing (17), (24), and (26), we have $\mathbb{E}_{p_{\psi,\varphi'}^{\mathrm{3D}}}\{\omega_L(\psi,\varphi';\alpha,\beta)\} \leq \mathbb{E}_{p_{\psi,\varphi'}^{\mathrm{2D}}}\{\omega_L(\psi,\varphi';\alpha,\beta)\} \leq \omega_L^{\mathrm{max}}(\alpha,\beta)$. This means that having the fixed receiving array coplanar with the transmitting array helps to enhance the local spatial bandwidth at the center of the receiving array. Furthermore, the maximum or expectation of the local spatial bandwidth at point P depends solely on the solid angle α and increases with it.

III. EFFECTIVE SPATIAL BANDWIDTH, K NUMBER, AND EDOF ANALYSIS

In this section, we leverage the concept of local spatial bandwidth to examine the effective spatial bandwidth and the K number of the transmitting and receiving arrays in an XL-MIMO system. Specifically, we extend the definition of effective spatial bandwidth to scenarios where the transmitting and receiving arrays are positioned and oriented arbitrarily. By employing the approach used for solving local spatial bandwidth, we obtain a closed-form expression for the effective spatial bandwidth. Furthermore, based on the closedform expression for local spatial bandwidth, we derive an approximate closed-form expression for the K number, which represents the theoretical maximum spatial DoF achievable by large arrays under ideal conditions [17]. This allows a better understanding of the impact of array positioning and orientation on the EDoF in a LoS channel in a similar manner to how we understand the local spatial bandwidth at the center of the receiving array.

A. Effective Spatial Bandwidth

Note that the local spatial bandwidth for a given position at \mathcal{L}_p is obtained in (15). However, the spatial bandwidth of the entire receiving array should collect all the spatial frequencies

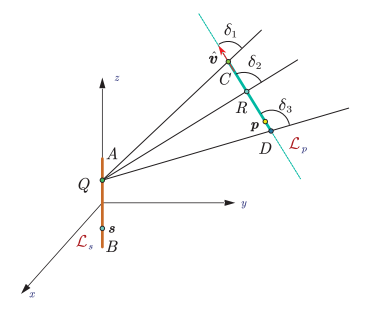


Fig. 7: Geometric relationship between the transmitting and receiving arrays.

obtained by all the positions at \mathcal{L}_p . Based on [24], we propose a definition for the effective spatial bandwidth for transmitting and receiving arrays with arbitrary positions and orientations.

Definition 3. The *effective spatial bandwidth* of \mathcal{L}_p is defined as the range of spatial frequencies that \mathcal{L}_p can receive, given by

$$\omega_{E}(\mathcal{L}_{p}) = k_{0} \left(\max_{\boldsymbol{p} \in \mathcal{L}_{p}, \boldsymbol{s} \in \mathcal{L}_{s}} \hat{\boldsymbol{r}}^{T} \left(\boldsymbol{p}, \boldsymbol{s} \right) \hat{\boldsymbol{v}} - \min_{\boldsymbol{p} \in \mathcal{L}_{p}, \boldsymbol{s} \in \mathcal{L}_{s}} \hat{\boldsymbol{r}}^{T} \left(\boldsymbol{p}, \boldsymbol{s} \right) \hat{\boldsymbol{v}} \right).$$
(27)

In contrast to local spatial bandwidth, effective spatial bandwidth depends not only on the relative position and orientation of the receiving array but also on its dimension. The local spatial bandwidth at the center of the receiving array is included within the effective spatial bandwidth, thus $\omega_E > \omega_L$. The effective spatial bandwidth of the transmitting array can be defined similarly, and thus omitted for brevity. Note that the effective spatial bandwidth defined in [24] is a special case when the transmitting and receiving arrays are in parallel.

Next, we provide the method for calculating the effective spatial bandwidth. As shown in Fig. 7, let the endpoints of \mathcal{L}_s be A and B, and the endpoints of \mathcal{L}_p be C and D. The orientation of \mathcal{L}_p is denoted by \hat{v} . Q is an arbitrary point on line segment AB, and point R is an arbitrary point on line segment CD (both including endpoints). δ_1 , δ_2 , δ_3 are the angles between the propagation direction vectors corresponding to the vectors \overrightarrow{QC} , \overrightarrow{QR} , \overrightarrow{QD} , and \hat{v} . According to geometric relationships, it follows that $\delta_1 \leq \delta_2 \leq \delta_3$.

Therefore, regardless of the location of Q within AB, the point p on the receiving array that maximizes the received spatial frequency is always at point C, while the point that minimizes the received spatial frequency is always at point D. Since Q and R are chosen arbitrarily, the maximum and minimum spatial frequencies received by \mathcal{L}_p are given by

$$\max_{\boldsymbol{p}\in\mathcal{L}_{p},\boldsymbol{s}\in\mathcal{L}_{s}} \hat{\boldsymbol{r}}^{\mathrm{T}}\left(\boldsymbol{p},\boldsymbol{s}\right) \hat{\boldsymbol{v}} = \max_{\boldsymbol{s}\in\mathcal{L}_{s}} \hat{\boldsymbol{r}}^{\mathrm{T}}\left(\boldsymbol{p}_{0} + \frac{L_{p}}{2}\hat{\boldsymbol{v}},\boldsymbol{s}\right) \hat{\boldsymbol{v}} \triangleq F_{C}^{\mathrm{max}},$$

$$\min_{\boldsymbol{p}\in\mathcal{L}_{p},\boldsymbol{s}\in\mathcal{L}_{s}} \hat{\boldsymbol{r}}^{\mathrm{T}}\left(\boldsymbol{p},\boldsymbol{s}\right) \hat{\boldsymbol{v}} = \min_{\boldsymbol{s}\in\mathcal{L}_{s}} \hat{\boldsymbol{r}}^{\mathrm{T}}\left(\boldsymbol{p}_{0} - \frac{L_{p}}{2}\hat{\boldsymbol{v}},\boldsymbol{s}\right) \hat{\boldsymbol{v}} \triangleq F_{D}^{\mathrm{min}},$$
(29)

where F_C^{\max} and F_D^{\min} denote the maximum spatial frequency at C and the minimum spatial bandwidth at D, respectively. Therefore, the effective spatial bandwidth between \mathcal{L}_s and \mathcal{L}_p can be expressed in closed form as

$$\omega_E = F_C^{\text{max}} - F_D^{\text{min}}. (30)$$

Note that the maximum and minimum spatial frequency for a given location have been provided in (13) and (14), respectively. This method allows for rapid and accurate identification of the effective spatial bandwidth, thereby accelerating system simulations.

In particular, when the transmitting and receiving arrays are parallel, it can be readily shown that the direction propagation vectors corresponding to the maximum and minimum spatial frequencies receivable by the arrays are achieved at the endpoints of the arrays. Consequently, the effective spatial bandwidths of the transmitting and receiving arrays are equal in this configuration. However, this property does not necessarily hold when the transmitting and receiving arrays are not parallel.

B. K Number

With local spatial bandwidth, the number of samples provided by non-redundant Nyquist sampling (i.e., denoted as K number [16]) can be computed using numerical or approximate methods. Since the K number provides an approximate estimate of the EDoF in MIMO channels, it offers a crucial theoretical foundation for the design and optimization of MIMO systems [17], [18]. Our objective is to derive a closed-form expression for the K number and utilize this expression to obtain a deeper understanding of how array geometry affects the EDoF of the channel.

According to [17], [26], for a 1D receiving array, the K number can be calculated as

$$K = \frac{1}{2\pi} \int_{-L_p/2}^{L_p/2} \omega_{\hat{\boldsymbol{v}}} \left(\boldsymbol{p}_0 + l_p \hat{\boldsymbol{v}}, \mathcal{L}_s \right) dl_p, \tag{31}$$

where $\omega_{\hat{v}} (p_0 + l_p \hat{v}, \mathcal{L}_s)$ denotes the local spatial bandwidth at the receiving array \mathcal{L}_p located at $p_0 + l_p \hat{v}$ when \mathcal{L}_p is oriented along \hat{v} . It can be observed that a larger K number corresponds to a richer set of plane wave components from \mathcal{L}_s received at \mathcal{L}_p (i.e., a larger spatial bandwidth). Since we have obtained a closed-form expression for the local spatial bandwidth at any point in 3D space, the K number can be efficiently approximated using a numerical method.

Consider the case of relatively small L_p compared to R, the local spatial bandwidth at different points across \mathcal{L}_p is approximately equal. Therefore, the local spatial bandwidth at the center of \mathcal{L}_p , denoted as $\omega_{\hat{v}}$ (p_0, \mathcal{L}_s), can serve as an approximation for the local spatial bandwidth at all points on \mathcal{L}_p . Then, the K number can be approximated as:

$$\tilde{K} = \frac{L_p}{2\pi} \omega_{\hat{\boldsymbol{v}}} \left(\boldsymbol{p}_0, \mathcal{L}_s \right). \tag{32}$$

In this case, the K number is proportional to the local spatial bandwidth $\omega_{\hat{v}}$ (p_0, \mathcal{L}_s) at the center of the array and the length L_p of the receiving array. Therefore, the properties of the local spatial bandwidth at the center of the receiving array obtained in Section II can be effectively leveraged for the analysis of channel EDoF. For example, the orientation \hat{v} that maximizes the K number of the receiving array \mathcal{L}_p is approximately equal to the orientation \hat{v} that maximizes the local spatial bandwidth at the center of \mathcal{L}_p . According to Proposition 1, the maximum value of the K number can be approximated as

$$\tilde{K}^{\max} = \frac{k_0 L_p}{\pi} \sin\left(\alpha/2\right). \tag{33}$$

C. Typical Case Study

For a typical and practical scenario where the transmission distance R is larger than the apertures of \mathcal{L}_s and \mathcal{L}_p , we provide approximations and simplifications for the local spatial bandwidth and the K number. Specifically, two cases are presented respectively: \mathcal{L}_s and \mathcal{L}_p are coplanar and \mathcal{L}_s and \mathcal{L}_p are non-coplanar.

1) \mathcal{L}_s and \mathcal{L}_p are coplanar: As shown in Fig. 8, let Ω be the plane containing both \mathcal{L}_s and \mathcal{L}_p , with the centers of \mathcal{L}_s and \mathcal{L}_p denoted as O and P, respectively. OM is the axis of \mathcal{L}_s . The line connecting O and P is denoted as l, and the length of the segment OP is R. In the plane Ω , let l_\perp be the perpendicular bisector of the line l. The angles between \mathcal{L}_s and l_\perp and between \mathcal{L}_p and l_\perp are denoted as θ and θ , respectively, where $\theta \in [0, \pi/2]$ and $\theta \in [0, \pi/2]$. Denote the angle subtended by P and the two ends of \mathcal{L}_s as $\angle APB = \alpha$. When $R \gg L_s$, we have $PA \approx PB$. Since AO = BO, according to the angle bisector theorem, we have $\angle APO \approx \angle BPO$, meaning that l can be approximated as the angle bisector of α . Therefore, we have $\varphi' \approx \pi/2 - \theta$. Additionally, since α is small when $R \gg L_s$, based on geometric relations, we have $\alpha \approx L_s \cos \theta/R$.

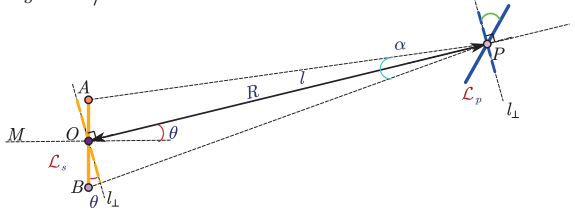


Fig. 8: Coplanar transmitting and receiving arrays. Substituting $\varphi' \approx \pi/2 - \vartheta$, $\psi = \pi/2$, and $\alpha \approx L_s \cos \theta/R$ into (15), the local spatial bandwidth at point P can be approximately expressed as

$$\tilde{\omega}_{2D} = 2k_0 \sin\left(\frac{\alpha}{2}\right) \sin\left(\frac{\pi}{2} - \vartheta\right) \\ \approx 2k_0 \cdot \frac{\alpha}{2} \cos \vartheta \approx k_0 \frac{L_s \cos \theta \cos \vartheta}{R}.$$
 (34)

Consequently, when $L_p \ll R$, the K number can be approximately expressed as

$$\tilde{K}_{2D} = \tilde{\omega}_{2D} L_p = k_0 \frac{L_s \cos \theta \cdot L_p \cos \theta}{R} \triangleq k_0 \frac{L_s' L_p'}{R},$$
 (35)

where $L_s' = L_s \cos \theta$ and $L_p' = L_p \cos \vartheta$ represent the projection lengths of \mathcal{L}_s and \mathcal{L}_p on l_\perp , respectively. From (35), we see that when the distance between the transmitting and receiving arrays is much larger than their respective sizes, the K number is proportional to the projection length of the transmitting and receiving arrays on l_\perp .

As shown in Fig. 9, when point P lies on the axis OM of \mathcal{L}_s , i.e., when $\theta=0$. In Fig. 9a, when the transmitting and receiving arrays are parallel (i.e., $\vartheta=\pi/2$), the K number is maximized, reaching $K\approx k_0\frac{L_sL_p}{R}$. At this point, the EDoFs of the channel are also maximized. Conversely, as depicted in Fig. 9b, when the transmitting and receiving arrays are perpendicular (i.e., $\vartheta=0$), the K number is minimized, approaching zero.

However, as shown in Fig. 10, when point P is not on the axis OM, it is surprising that the orientation of \mathcal{L}_p that

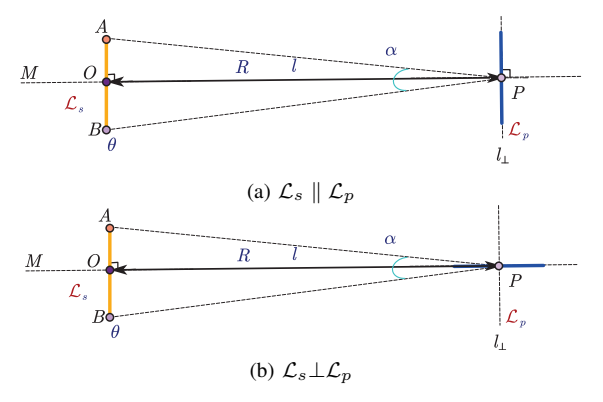


Fig. 9: Orientations of \mathcal{L}_p that maximize and minimize the K number when the center P of \mathcal{L}_p is on the axis OM of \mathcal{L}_s .

maximizes the K number is not parallel to \mathcal{L}_s , but rather perpendicular to the line l connecting the centers of \mathcal{L}_p and \mathcal{L}_s (Fig. 10a). In this orientation, \mathcal{L}_p receives a richer set of plane wave components, and the maximum K number is given by $K \approx k_0 \frac{L_s' L_p}{R}$. Similarly, the orientation of \mathcal{L}_p that minimizes the K number is not perpendicular to \mathcal{L}_s , but aligned with the line l connecting the centers of \mathcal{L}_p and \mathcal{L}_s (Fig. 10b). In this case, the K number approaches its minimum value, close to zero, and the channel's EDoFs are also minimized. Therefore, by merely controlling the orientation of the receiving array, we can freely adjust the K number within the range $[0, k_0 \frac{L_s L_p}{R}]$.

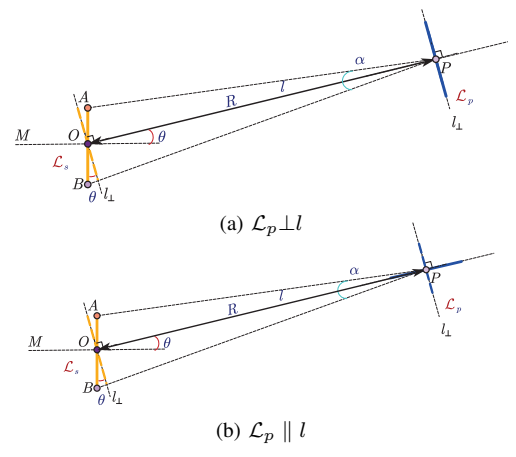


Fig. 10: The orientations of \mathcal{L}_p that maximize and minimize the K number when the center P of \mathcal{L}_p is not on the axis OM of \mathcal{L}_s .

2) \mathcal{L}_s and \mathcal{L}_p are non-coplanar: As shown in Fig. 11, assume that the transmitting array \mathcal{L}_s and the receiving array \mathcal{L}_p are not coplanar. Let the plane containing points A, B, and P be denoted as Ω , with \hat{n}_t representing the normal vector of plane Ω . Define the angle between \hat{n}_t and \mathcal{L}_p as $\pi/2 - \phi$, where $\phi \in [0, \pi/2]$. Consequently, we have $\psi = \pi/2 - \phi$.

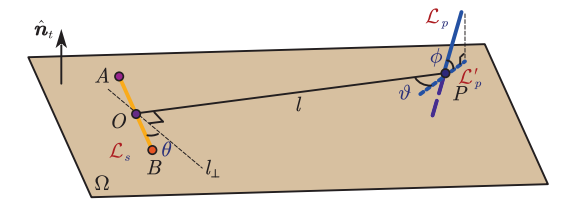


Fig. 11: Non-coplanar transmitting and receiving arrays.

Similar to (34), when $R \gg L_s$, the local spatial bandwidth at point P can be approximately expressed based on the geometric relationships and (15):

$$\tilde{\omega}_{3D} = k_0 \frac{L_s \cos \theta \sin \theta \cos \phi}{R}.$$
 (36)

When $L_p \ll R$, the K number can be approximately expressed as:

$$\tilde{K}_{3D} = \tilde{\omega}_{3D} L_p = k_0 \frac{L_s \cos \theta \cdot L_p \sin \theta \cos \phi}{R} \triangleq k_0 \frac{L_s' L_p''}{R},$$
(37)

where L_p'' denotes the projection length of \mathcal{L}_p onto l_\perp after being projected onto Ω as \mathcal{L}_p' . Note that (37) shares the same form as the spatial DoFs presented in [22], [27]. Clearly, for fixed array distance R and angle θ , \tilde{K}_{3D} reaches its maximum value when $\phi=0$ and $\vartheta=\pi/2$ (i.e., when \mathcal{L}_s and \mathcal{L}_p are coplanar and $\mathcal{L}_p \perp l$). Conversely, when $\phi=\pi/2$ (i.e., when $\mathcal{L}_p \perp \Omega$, as shown in Fig. 12), the approximate spatial bandwidth $\tilde{\omega}_{3D}$ is nearly zero, resulting in $\tilde{K}_{3D}\approx 0$. Therefore, to enhance the EDoF of the channel, the transmitting and receiving antennas should ideally be positioned within the same plane.

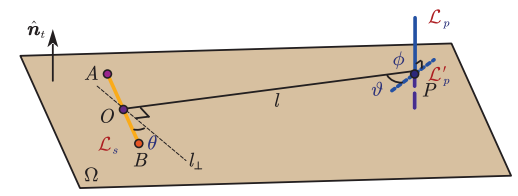


Fig. 12: Non-coplanar perpendicular transmitting and receiving arrays.

D. Numerical Validations

We first provide the numerical validations of the relationship between the effective spatial bandwidth of the array and its position and orientation, and analyze the approximation accuracy of the K number. Subsequently, using a discrete aperture array as an example, we reveal the physical meaning of effective spatial bandwidth from the perspective of plane wave decomposition and demonstrate the relationship between the K number and the EDoF of the channel.

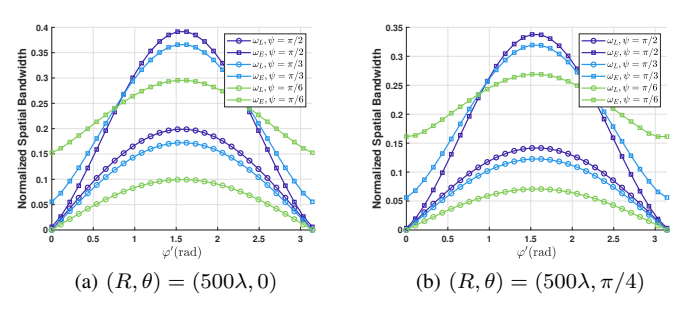


Fig. 13: The relationship between the normalized local spatial bandwidth and the normalized effective spatial bandwidth.

Fig. 13 illustrates the relationship between the normalized effective spatial bandwidth ω_E/k_0 and the normalized local spatial bandwidth ω_L/k_0 at the center of \mathcal{L}_p with respect to the orientation (ψ,φ') of \mathcal{L}_p , given $L_s=L_p=100\lambda$. It can be observed that both the local spatial bandwidth and the

effective spatial bandwidth first increase and then decrease as φ' increases, reaching their maximum values around $\varphi=\pi/2$. Moreover, the variation trend of the effective spatial bandwidth with φ' is consistent with that of the central local spatial bandwidth. When $\psi=0$, the local spatial bandwidth at the center of \mathcal{L}_p is zero, but the effective spatial bandwidth remains non-zero.

Fig. 14 illustrates the relationship between the K number and the orientation of the receiving array \mathcal{L}_p , when $L_s=100\lambda,\ L_p=100\lambda,\$ and $\lambda=0.01$ m. The K number is calculated using both numerical methods ("Num.") and the approximation method ("Approx.") as given in (32). It can be observed that the K number reaches its approximate maximum when the local spatial bandwidth of the \mathcal{L}_p center is maximized, i.e., when $\varphi'=\pi/2$. Additionally, the K number computed via (32) is approximately equal to that obtained using the numerical method, thereby validating the accuracy of the approximation in equation (32). It is also noted that when $\psi=0$, the local spatial bandwidth of the receiving array is zero. However, the K number is generally non-zero, but it remains close to zero.

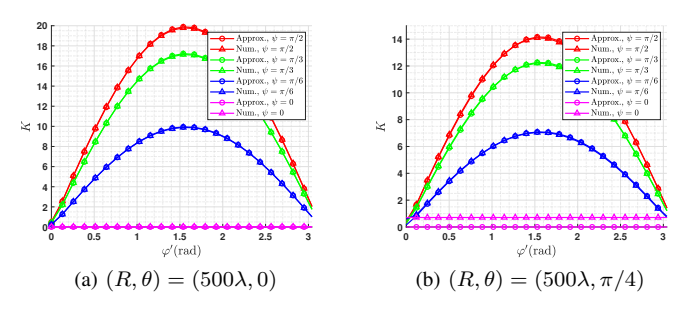


Fig. 14: K number for different orientations of the receiving array.

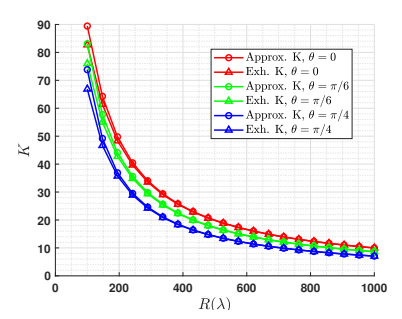
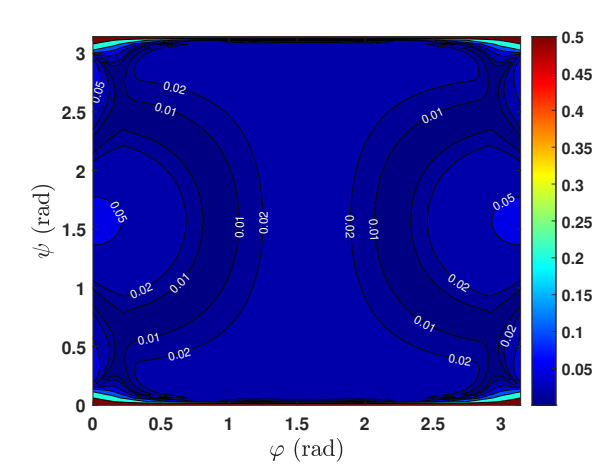


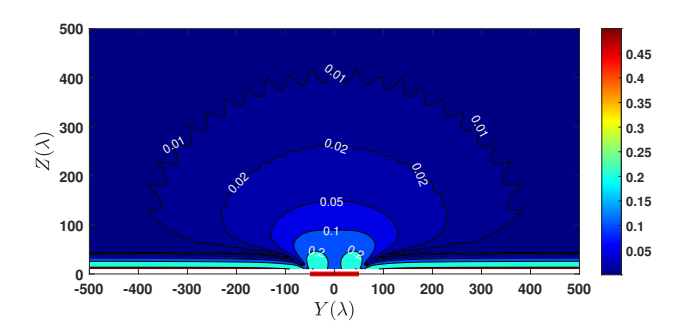
Fig. 15: The maximum K number vs. receiving positions.

Fig. 15 illustrates the relationship between the position of the receiving array \mathcal{L}_p and its maximum K number when $L_s=100\lambda,\ L_p=100\lambda,\$ and $\lambda=0.01$ m. "Approx. K" represents the maximum value of the K number calculated using (33). "Exh. K" denotes the K number calculated using numerical methods and then maximized by traversing all possible receiving directions \hat{v} . As shown in Fig. 15, the maximum K number decreases monotonically with increasing distance R between the transmitting and receiving arrays, and the rate of decrease diminishes monotonically as well. The maximum K number also decreases monotonically with increasing θ . When $\theta=0$, the maximum K number reaches its peak. Additionally, it is observed that the maximum K

number calculated via (33) closely matches the maximum K number obtained numerically, particularly when $R>300\lambda$. This validates the accuracy of the approximate expression for the K number provided by (32) and (33).



(a) Approximation error of the K number under different orientations of the receive array.



(b) Approximation error of the maximum K number.

Fig. 16: Normalized computation error of the K number. The normalized computation error of the K number is

defined as $\epsilon = |\tilde{K} - K|/K$, where K is obtained via numerical integration. Fig. 16a illustrates the approximation error of the K number when the receive array \mathcal{L}_p adopts various orientations (ψ, φ) , under the configuration $L_s = L_p = 100\lambda$, $R = 200\lambda$, and $\theta = 0$. As observed from the figure, even when the transmitter-receiver distance is on the same order of magnitude as the array dimensions, the approximation error remains below 5% for most receive array orientations. Fig. 16b illustrates the approximation error of the maximum Knumber, where \tilde{K}^{\max} denotes the maximum value obtained via (33). In this setup, $L_s = L_p = 100\lambda$, the transmit array is fixed at the location marked by the red line segment, and the receive array is placed at each position across the plane. The results demonstrate that as the separation between the transmit and receive arrays increases, the approximation error of the maximum K number decreases. When the separation

Next, we illustrate the application of effective spatial bandwidth and the K number using a discrete aperture array as

exceeds 200λ , the approximation error remains below 5% in

most regions. These results validate the effectiveness of the

proposed approximation method.

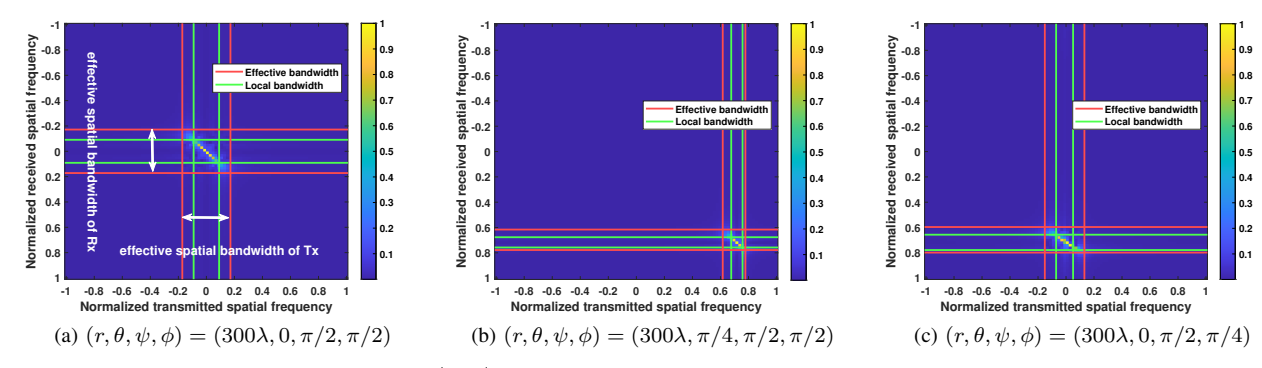


Fig. 17: Illustration of $|\mathbf{H}^a|$, local spatial bandwidth, and effective spatial bandwidth.

an example. Specifically, we consider the case where both the transmitting and receiving arrays are uniform linear arrays (ULAs). Let the antenna spacing of the transmitting array \mathcal{L}_s and the receiving array \mathcal{L}_p be Δ_s and Δ_p , respectively. Consequently, the numbers of transmitting antennas and receiving antennas are $N_t = L_s/\Delta_s + 1$ and $N_r = L_p/\Delta_p + 1$, respectively. Let the MIMO channel be represented by $\mathbf{H} \in \mathbb{C}^{N_r \times N_t}$. Considering the near-field spherical wavefront effect [24], [28], the complex gain between the n_r -th receiving antenna and the n_t -th transmitting antenna can be modeled as

$$h_{n_r,n_t} = [\mathbf{H}]_{n_r,n_t} = \frac{\lambda}{4\pi r_{n_r,n_t}} e^{jk_0 r_{n_r,n_t}}, \qquad (38)$$

where r_{n_r,n_t} denotes the distance between the n_r -th receiving antenna and the n_t -th transmitting antenna, with $n_r = 1, \ldots, N_r$ and $n_t = 1, \ldots, N_t$.

Applying Fourier plane wave decomposition to the near-field spherical wave channel results in an angular-domain (or wavenumber-domain) channel \mathbf{H}^a with a sparse structure [24]:

$$\mathbf{H}^{a} = \frac{1}{\sqrt{N_{t}N_{r}}} \mathbf{A}_{R}^{H} \mathbf{H} \mathbf{A}_{T}, \tag{39}$$

where $\mathbf{A}_R \in \mathbb{C}^{N_r \times N_r}$ and $\mathbf{A}_T \in \mathbb{C}^{N_t \times N_t}$ represent the receiving and transmitting array response matrices, respectively, both of which are discrete DFT matrices. Specifically, each column vector of \mathbf{A}_R and \mathbf{A}_T represents a wavenumber-domain codeword corresponding to a specific spatial frequency.

Fig. 17 illustrates the normalized magnitude of the LoS XL-MIMO angular-domain channel $|\mathbf{H}^a|$, when $\Delta_s = \Delta_t = \frac{\lambda}{2}$ and $N_t = N_r = 100$. The position and orientation of the receiving array are described by the quadruple $(r, \theta, \psi, \varphi)$. It can be observed that the angular-domain channel exhibits sparsity, with almost all the energy concentrated within a continuous range of transmit/receive spatial frequencies. This range is referred to as the effective spatial bandwidth of the transmitter/receiver. The red line represents the effective spatial bandwidth calculated using (30). The plane wave components within the effective spatial bandwidth are sufficient to characterize the LoS XL-MIMO channel, which implies low-overhead channel estimation and low-complexity transmission schemes.

Note that in Fig. 17a, the effective spatial bandwidths of the transmitting and receiving arrays are equal. As shown in Fig. 17b, if the transmitting and receiving arrays remain parallel, the effective spatial bandwidths are still equal but noticeably reduced in size. Fig. 17c demonstrates that when the azimuth

angle of the receiving array is changed, the effective spatial bandwidths of both arrays decrease, and since they are no longer parallel, their effective spatial bandwidths are no longer equal.

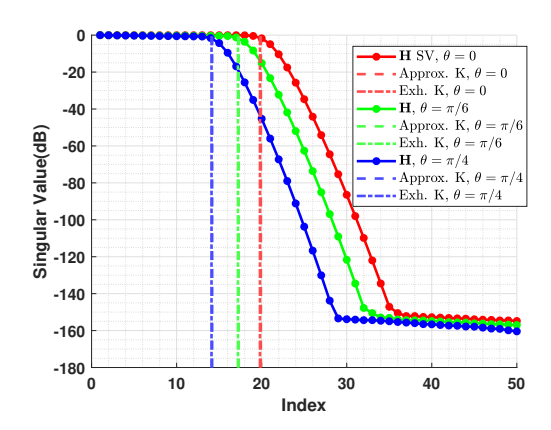


Fig. 18: Singular values of the LoS XL-MIMO channel and the K number vs. different receiving positions.

Fig. 18 illustrates the distribution of normalized singular values of the channel **H** when $L_s = L_p = 100\lambda$, $R = 500\lambda$, $\Delta_s = \Delta_p = \lambda/2$, and $\lambda = 0.01$ m. The meanings of "Approx. K" and "Exh. K" are the same as in Fig. 15. "H SV" represents the distribution of normalized singular values of the channel matrix H under the receiving orientation corresponding to "Exh. K". Let the ordered singular values of H be denoted as $\sigma_1 \geq \sigma_2 \geq \cdots \geq \sigma_N$. As seen in Fig. 18, regardless of the position of the receiving array \mathcal{L}_p , the rate of decrease of σ_n can always be divided into two stages: in the first stage, the singular values σ_n remain roughly constant until reaching a critical threshold, after which σ_n rapidly decays. Therefore, the main energy of the channel is concentrated on the eigenmodes before the threshold. In fact, this "threshold" is referred to as the EDoF, which is related to the spatial multiplexing capability of MIMO communication [10]. Fig. 18 also shows that "Exh. K" can effectively delineate the two stages of singular value decay, validating that the K number is a good approximation of the EDoF. Additionally, we observe that "Approx. K" and "Exh. K" almost overlap, which validates the correctness of (32) and (33). Meanwhile, we observe that for the same R, the larger the θ , the smaller the K number and the EDoF of H. This conclusion aligns with the properties of local spatial bandwidth shown in Fig. 6 and Fig. 15.

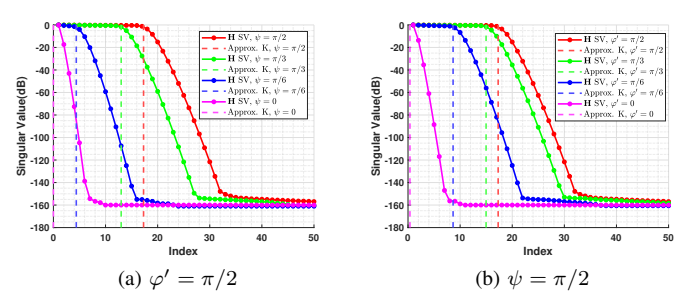


Fig. 19: Singular values of the LoS XL-MIMO channel and the K number vs. different receiving orientations.

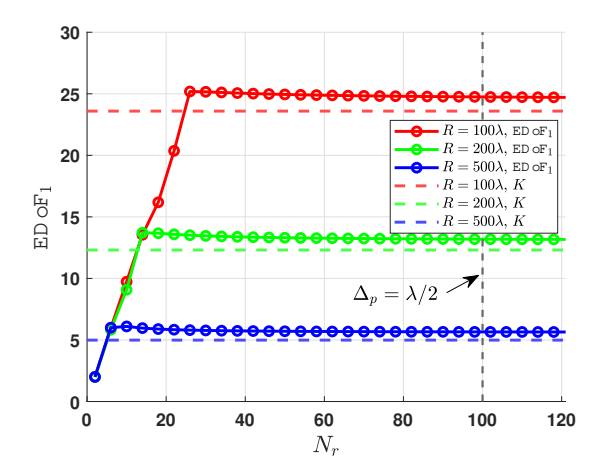


Fig. 20: EDoF₁ versus the number of receiving antennas N_t .

Fig. 19 illustrates the relationship between the normalized singular value distribution of the channel matrix H and the orientation of the receiving array (ψ, φ') . The parameters are set as $L_s = L_p = 100\lambda$, $(R, \theta) = (500\lambda, \pi/6)$, $\Delta_s = \Delta_p = \lambda/2$, and $\lambda = 0.01 \text{m}$. Fig. 19a examines the EDoF of the channel matrix **H** when $\varphi' = \pi/2$ and ψ varies in the range $[0, \pi/2]$. "H SV" denotes the singular value distribution of the channel matrix **H** for the receiving array orientation (ψ, φ') . "Approx. K" represents the approximate K number calculated using (32). It can be observed that when $\psi = \pi/2$ (i.e., when \mathcal{L}_s and \mathcal{L}_p are coplanar), both the K number and the EDoF of the channel reach their maximum values. Conversely, when $\psi = 0$ (i.e., when \mathcal{L}_p is perpendicular to \mathcal{L}_s), the K number and the EDoF are minimized. Similarly, Fig. 19b investigates the EDoF of the channel matrix **H** when $\psi = \pi/2$ and φ' varies in the range $[0, \pi/2]$. It is found that when $\varphi' = \pi/2$ (i.e., when \mathcal{L}_p is perpendicular to the centerline of the transmitting and receiving arrays), the K number and EDoF of the channel reach their maximum values. When $\varphi'=0$ (i.e., when \mathcal{L}_p is collinear with the centerline of the transmitting and receiving arrays), the K number and EDoF are minimized.

To further investigate the impact of antenna spacing on the EDoF, Fig. 20 illustrates the relationship between EDoF₁ and the number of receive antennas N_r , under the configuration where the transmit and receive array apertures are fixed as $L_s=L_p=100\lambda$, with transmit antenna spacing $\Delta_s=\lambda/2$, and angular parameters $\theta=0,\ \psi=\pi/2$, and $\varphi'=\pi/2$. The value of EDoF₁ is computed as EDoF₁ =

 $(\operatorname{tr}(\mathbf{H}\mathbf{H}^H)/\|\mathbf{H}\mathbf{H}^H\|_F)^2$, which serves as an approximation of the EDoF [10]. R denotes the distance between the transmit and receive arrays. The gray dashed line marks the number of receive antennas when the spacing across the aperture \mathcal{L}_p reaches half a wavelength. As shown in the Fig. 20, EDoF₁ increases with N_r (i.e., as the antenna spacing Δ_p decreases), and gradually approaches a stable value. This value can be well approximated by the K number, which is determined by the array geometry. When R increases, the convergence becomes faster. These results indicate that the maximum achievable EDoF is limited by the array geometry, such as the aperture size and antenna arrangement. The K number, which depends only on the array configuration, can be used to estimate this limit. When the antenna spacing is reduced to half a wavelength or less, the EDoF becomes close to its theoretical maximum, and further increasing the number of antennas brings little improvement. In some cases, even when the antenna spacing is larger than half a wavelength, the EDoF can still reach its theoretical limit, as long as the spatial sampling condition is satisfied.

IV. IMPACT OF ARRAY GEOMETRY ON CHANNEL CAPACITY

In this section, building upon the relationships between array geometry, spatial bandwidth, K number, and EDoF discussed in the previous sections, we analyze the impact of array geometry on LoS XL-MIMO channel capacity. Unlike the method in [28], which approximates the channel's active DoF using Taylor expansion and inductive reasoning to derive an upper bound on capacity, this paper introduces a framework for analyzing channel capacity from the perspective of spatial bandwidth and K number.

A. Theoretical Analysis

As illustrated in Fig. 21, we consider both the transmitting and receiving antenna arrays to be ULA, each comprising N_t and N_r antennas, respectively, operating over a LoS channel represented by $\mathbf{H} \in \mathbb{C}^{N_r \times N_t}$. Considering spherical wave effects, the complex gain $h_{m,n}$ between the m-th receiving antenna and the n-th transmitting antenna is given by

$$h_{m,n} = [\mathbf{H}]_{m,n} = \frac{\sqrt{G_t G_r} \lambda}{4\pi r_{m,n}} e^{-jk_0 r_{m,n}},$$
 (40)

where G_t and G_r denote the antenna gains of the transmitting and receiving antennas, respectively. $r_{m,n}$ represents the distance between the m-th receiving antenna and the n-th transmitting antenna. Considering the dimensions of the transmitting and receiving arrays are relatively small compared to their distance, we can approximate $r_{m,n} \approx R$, where R is the distance between the centers of the transmitting and receiving antenna arrays. Therefore, the magnitude of the complex gain $h_{m,n}$ can be considered constant, focusing only on the phase variation across different antenna pairs 5 .

⁵The approximation of the inter-element distance in the transmitting and receiving arrays is used only for simplifying the derivation, while the channel model in (40) is still used in the numerical simulations.

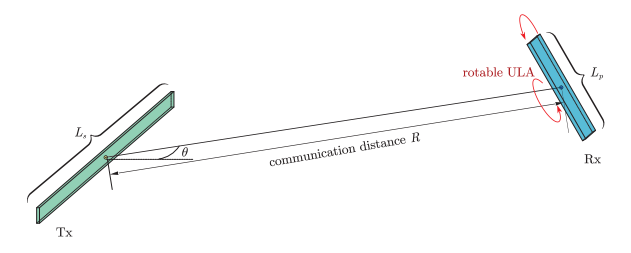


Fig. 21: Rotatable ULA for LoS XL-MIMO Transmission.

This LoS XL-MIMO system can be represented as

$$y = Hx + w \tag{41}$$

where $\mathbf{x} \in \mathbb{C}^{N_t}$ and $\mathbf{y} \in \mathbb{C}^{N_r}$ denote the transmit signal vector and receive signal vector, respectively. $\mathbf{w} \sim \mathcal{CN}(0, N_0 \mathbf{I}_{N_r})$ represents additive white Gaussian noise (AWGN) at the receiver. The total power constraint on the transmitted signals is $P_t = \|\mathbf{x}\|^2$.

For simplicity, the positions and orientations of the transmitting array are fixed, while the orientation of the receiving array can be adjusted. We only consider the impact of the receiving orientation \hat{v} on the channel capacity. The adjustment of array orientation can be achieved using next-generation reconfigurable antenna (NGRA) technologies, such as [29], [30]. The LoS channel is entirely determined by \hat{v} , denoted as $\mathbf{H} \triangleq \mathbf{H}(\psi, \varphi)$, where (ψ, φ) describe the elevation and azimuth angles of the receiving array orientation, consistent with the definitions in Section II.

The information-theoretic capacity of H is

$$C(\mathbf{H}, \text{SNR}) = \max_{\sum_{i=1}^{N_{\min}} p_i = P_t, \ p_i \ge 0} \sum_{i=1}^{N_{\min}} \log_2 \left(1 + \frac{p_i \sigma_i^2}{N_0} \right)$$
$$= \sum_{i=1}^{N_{\min}} \log_2 \left(1 + \frac{p_i^* \sigma_i^2}{N_0} \right), \tag{42}$$

where $N_{\min} = \min\{N_t, N_r\}$. $\sigma_1 \ge \sigma_2 \ge \cdots \ge \sigma_{N_{\min}}$ are the ordered singular values of the channel matrix **H**, with each σ_i corresponding to an eigenmode of the sub-channel, satisfying:

$$\sum_{i=1}^{N_{\min}} \sigma_i^2 = \operatorname{Tr}\left(\mathbf{H}\mathbf{H}^{\mathrm{H}}\right) = \|\mathbf{H}\|_F^2. \tag{43}$$

And p_i represents the power allocated to sub-channel i obtained via the water-filling algorithm:

$$p_i^* = \left[\mu - \frac{N_0}{\sigma_i^2}\right]^+. \tag{44}$$

When adjusting the orientation (ψ, φ) of the receiving array, the distribution of the singular values of the channel **H** changes, thereby affecting the optimal power allocation p_i^* and ultimately influencing the channel capacity. Furthermore, from (44), it is observed that the receiving SNR ratio also impacts the optimal power allocation p_i^* .

We consider the following problem: adjusting the orientation (ψ,φ) of the receiving antenna to maximize the channel capacity C under different SNR:

$$C\left(\text{SNR}\right) = \max_{0 \le \psi \le \pi, 0 \le \varphi \le \pi} C\left(\mathbf{H}\left(\psi, \varphi\right), \text{SNR}\right). \tag{45}$$

Problem (45) can be solved by exhaustively searching all possible orientations of the receiving antenna, but this approach has high computational complexity. By leveraging our previous analysis of spatial bandwidth, *K* number, and EDoF in the bilateral near-field scenario, we can simplify the analysis and derive some interesting conclusions. Specifically, we consider this issue in two cases: the far-field and the near-field, as each leads to different conclusions.

1) Far-Field LoS XL-MIMO Channel: Under the far-field assumption, the distance R between the transmitting and receiving antennas is much greater than the product of their apertures. According to (37), the K number is approximately zero, resulting in \mathbf{H} having only one EDoF. The main energy of the far-field channel is concentrated in the eigenmode corresponding to the largest singular value σ_1 , i.e., $\sigma_1^2 \approx \|\mathbf{H}\|_F^2$. According to (44), all power should be allocated to the eigenmode corresponding to the largest singular value σ_1 . Thus, the far-field channel capacity C^{FF} can be approximated as

$$C^{\text{FF}} \approx \log_2 \left(1 + \frac{P_t \|\mathbf{H}\|_F^2}{N_0} \right).$$
 (46)

Since $\|\mathbf{H}\|_F^2 \approx \frac{G_t G_r \lambda^2}{(4\pi R)^2} N_t N_r$, it is determined by the distance R between the transmitting and receiving arrays, as well as the number of transmitting and receiving antennas N_t and N_r , while it is independent of the orientation (ψ, φ) of the receiving antenna array. Therefore, adjusting the receiving antenna array orientation minimally benefits channel capacity, as far-field LoS XL-MIMO channels offer power gain but lack spatial multiplexing capability, rendering the LoS channel considered to be unfavorable for MIMO communication [7].

2) Near-Field LoS XL-MIMO Channel: Near-field LoS XL-MIMO can alter this rule. Based on the previous analysis of the singular value distribution of the near-field channel, it can be observed that the singular values of the near-field channel are primarily concentrated in the eigenmodes corresponding to $\sigma_1, \sigma_2, \cdots, \sigma_k$, where k represents the EDoF, such that $\sum_{i=1}^k \sigma_i^2 \approx \|\mathbf{H}\|_F^2$. In this case, the near-field channel capacity can be expressed as

$$C^{\text{NF}} \approx \max_{\sum_{i=1}^{K} p_i = P_t} \sum_{i=1}^{k} \log_2 \left(1 + \frac{p_i \sigma_i^2}{N_0} \right).$$
 (47)

At this point, the orientation of the receiving array profoundly affects the power allocation among sub-channels by altering the distribution of the singular values of the channel matrix. Since the SNR impacts sub-channel power allocation, we will discuss the influence of the receiving array orientation on the near-field LoS XL-MIMO channel capacity under both high and low SNR conditions.

When the transmit power P_t is high and the SNR is high, the water-filling level μ in the channel's water-filling algorithm is also high. According to (44), an equal power allocation strategy for all non-zero eigenmodes becomes asymptotically optimal, and the channel capacity can be approximately expressed as

$$C_1^{\text{NF}} \approx \sum_{i=1}^k \log_2 \left(1 + \frac{P_t \sigma_i^2}{k N_0} \right) \approx k \log_2 \text{SNR} + \text{const}, \quad (48)$$

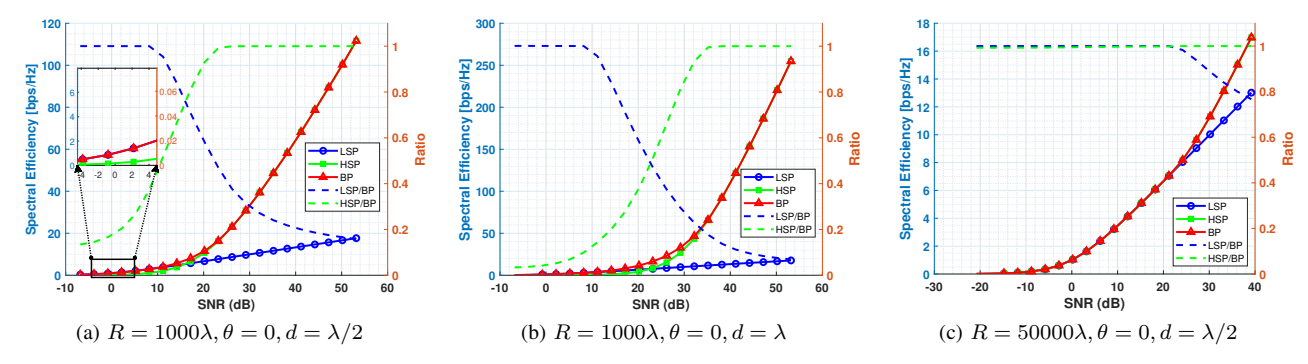


Fig. 22: Channel capacity under different receiving array configurations.

where SNR = P_t/N_0 is defined as the transmit SNR. The channel capacity scales logarithmically with SNR, proportional to the number of multiplexable streams k, which can be approximated by the K number. Note that the optimal receiving orientation (ψ_1, φ_1') for ULA arrays to maximize K (or EDoF) is provided in Section III. Applying this orientation in near-field high SNR scenarios maximizes channel capacity.

When the transmit power P_t is low and the SNR is low, the water-filling level μ in the channel's water-filling algorithm is also low. According to (44), allocating all power to the sub-channel corresponding to the strongest eigenmode σ_1 is optimal, i.e., $C_2^{\rm NF} \approx \log_2\left(1 + \frac{P_t\sigma_1^2}{N_0}\right)$. Unlike the high SNR scenario, where increasing the EDoF supports multiplexing, in the low SNR scenario, maximizing channel capacity requires concentrating the entire channel energy in the strongest eigenmode, such that $\sigma_1^2 \approx \|\mathbf{H}\|_F^2$, which necessitates minimizing the EDoF. In this case, the optimal receiving orientation is the one that minimizes the K number (or EDoF) for ULA arrays, as shown in Section III, denoted as (ψ_2, φ_2) . Using this receiving orientation in the near-field low SNR scenario can maximize channel capacity. This conclusion is somewhat surprising, as the optimal array orientation that maximizes channel capacity varies with different SNRs. The optimal receiving array orientation for high SNR is exactly perpendicular to the optimal orientation for low SNR.

As the transmission distance r increases, the maximum EDoF decreases (see (37)), diminishing the effect of receiving orientation on singular value distribution. Thus, the impact of array orientation on channel capacity gradually weakens from near-field to far-field. Near-field properties enable EDoF control, with array orientation serving as an effective approach.

B. Simulation Results

In this subsection, numerical simulations are presented. The working frequency is set to $f=30 \mathrm{GHz},~N_r=128$ and $N_t=256$, respectively. The transmitter is at the origin, with receiving antennas positioned at (R,θ) . We consider three receiving array configurations:

- **LSP**: Orientation minimizes *K*/EDoF, with the receiving array perpendicular to the transmitting array and on a different plane.
- HSP: Orientation maximizes K/EDoF, with the receiving array coplanar and perpendicular to the line connecting array centers.

• **BP**: Orientation maximizes spectral efficiency, selected via exhaustive search.

Performance is also compared using ratios "LSP/BP" and "HSP/BP", representing spectral efficiency ratios of "LSP" and "HSP" to "BP", respectively.

Fig. 22a illustrates the impact of array orientation on spectral efficiency at different receiving SNRs when $R=1000\lambda$, $\theta=0$, and $d=\lambda/2$. From Fig. 22a, it can be observed that the spectral efficiency increases with receiving SNR. Additionally, in the "LSP" scheme, spectral efficiency increases linearly with SNR, while in the "HSP" scheme, the growth rate accelerates as SNR increases. This occurs because higher SNR activates more DoF in the "HSP" channel, enabling spatial multiplexing, with the number of activated DoF proportional to the spectral efficiency slope. In contrast, the "LSP" channel, with limited EDoF, lacks spatial multiplexing gain, resulting in a linear, constant-slope increase in spectral efficiency with SNR.

In the low-SNR regime, the ratio "LSP/BP" ≈ 1 , verifying that the proposed orientation minimizing K can approximately maximize spectral efficiency. In the high-SNR regime, the ratio "HSP/BP" ≈ 1 , indicating that the orientation maximizing K achieves near-optimal spectral efficiency. However, "LSP/BP" drops below 20% in this regime, highlighting the importance of array orientation adjustment to enhance spatial multiplexing and improve capacity.

Fig. 22b presents the simulation results when the number of antennas in the transmitting and receiving arrays remains unchanged, but the antenna spacing is adjusted to $d=\lambda$ (doubling the array aperture). It can be observed that in the high-SNR regime, the spectral efficiency of the "LSP" scheme remains nearly unchanged compared to Fig. 22a, whereas that of the "HSP" scheme more than doubles. This is because the "HSP" scheme can effectively utilize spatial DoF to enhance channel capacity, whereas the "LSP" scheme cannot. It further emphasizes that increasing the array aperture is an effective way to enhance spatial DoF.

Fig. 22c illustrates the spectral efficiency under different schemes as the distance between the transmitting and receiving arrays increases. Comparing Figs. 22a and 22c, it is observed that the spectral efficiency decreases. Furthermore, "LSP/BP" and "HSP/BP" are almost equal to 1, meaning that the spectral efficiencies corresponding to different receiving array orientations are nearly the same. For far-field channels, the maximum K number is close to 0, so adjusting the orientation of the

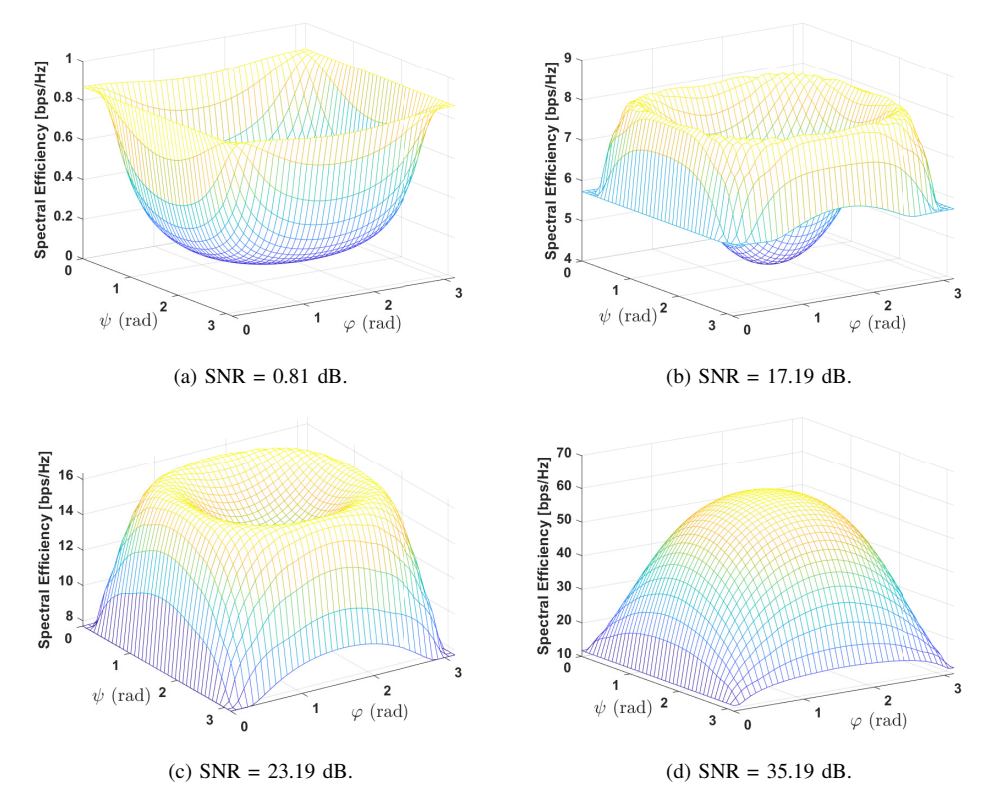


Fig. 23: Channel Capacity vs. receive array orientation at different SNRs.

receiving array has a minimal impact on the channel's EDoF. In other words, when considering the channel capacity of a far-field LoS XL-MIMO system, the impact of array orientation can be considered negligible.

We further investigate the spectral efficiency under various receive array orientations and different receiving SNR levels, assuming $R = 500\lambda$, $\theta = 0$, and $d = \lambda/2$, as illustrated in Fig. 23. The orientation of the receive array \mathcal{L}_p is parameterized by (ψ, φ) . Notably, in this configuration, the K number (or EDoF) reaches its maximum when $(\psi, \varphi) = (\pi/2, \pi/2)$. Interestingly, as shown in Fig. 23a, in the low-SNR regime, the orientation that maximizes the K number results in the lowest spectral efficiency. This phenomenon arises because the channel energy is spread across multiple eigenmodes, but only the strongest mode can be effectively utilized in the low-SNR regime. As the SNR increases, the orientation that achieves the highest spectral efficiency gradually shifts toward $(\pi/2, \pi/2)$ (see Fig. 23b and Fig. 23c). At high-SNR regime (see Fig. 23d), the orientation that maximizes the K number also yields the highest spectral efficiency, as more independent sub-channels can be effectively exploited for parallel data transmission. These results are consistent with the theoretical analysis presented in Section IV-A and highlight the importance of optimizing array orientation in near-field communication systems.

V. CONCLUSION

In this paper, we provided a closed-form expression for the local spatial bandwidth of the LoS channel with LSAAs

in 3D space. Furthermore, we obtained representations of effective spatial bandwidth and EDoF for the LoS XL-MIMO channel. Additionally, we have elaborated on how to adjust the spatial positions of the receiving array to improve the EDoF of the channel. Based on these derivations, the following interesting conclusions can be obtained: The maximum local spatial bandwidth at the center of the receiving array is related to the solid angle formed by the center of the receiving array and the ends of the transmitting array. When the transmitting and receiving arrays are coplanar, and both arrays are perpendicular to the line connecting the centers of the arrays, the channel's EDoF is maximized, which also maximizes the XL-MIMO channel capacity in high-SNR conditions. Conversely, when the transmitting and receiving arrays are perpendicular, the channel's EDoF is minimized, which maximizes the XL-MIMO channel capacity in low-SNR conditions.

REFERENCES

- D. Dardari, "Communicating with large intelligent surfaces: Fundamental limits and models," *IEEE J. Sel. Areas Commun.*, vol. 38, no. 11, pp. 2526–2537, 2020.
- [2] I. F. Akyildiz, C. Han, and S. Nie, "Combating the distance problem in the millimeter wave and terahertz frequency bands," *IEEE Commun. Mag.*, vol. 56, no. 6, pp. 102–108, 2018.
- [3] H. Lu and Y. Zeng, "Communicating with extremely large-scale array/surface: Unified modeling and performance analysis," *IEEE Trans. Wireless Commun.*, vol. 21, no. 6, pp. 4039–4053, 2021.
- [4] A. Tang, J.-B. Wang, Y. Pan, C. Zeng, Y. Chen, H. Yu, M. Xiao, R. C. De Lamare, and J. Wang, "Channel estimation for XL-MIMO systems with decentralized baseband processing: Integrating local reconstruction with global refinement," *IEEE Trans. Commun.*, 2025.

- [5] C. Zeng, J.-B. Wang, M. Xiao, C. Ding, Y. Chen, H. Yu, and J. Wang, "Task-oriented semantic communication over rate splitting enabled wireless control systems for URLLC services," *IEEE Trans. Commun.*, vol. 72, no. 2, pp. 722–739, 2024.
- [6] T. S. Rappaport, E. Ben-Dor, J. N. Murdock, and Y. Qiao, "38 GHz and 60 GHz angle-dependent propagation for cellular & peer-to-peer wireless communications," in *Proc. IEEE Int. Conf. Commun. (ICC)*, 2012, pp. 4568–4573.
- [7] D. Tse and P. Viswanath, Fundamentals of wireless communication. Cambridge university press, 2005.
- [8] A. Tang, J.-B. Wang, Y. Pan, W. Zhang, Y. Chen, H. Yu, and R. C. d. Lamare, "Spatially non-stationary XL-MIMO channel estimation: A three-layer generalized approximate message passing method," *IEEE Trans. Signal Process.*, vol. 73, pp. 356–371, 2025.
- [9] Y. Pan, C. Pan, S. Jin, and J. Wang, "RIS-aided near-field localization and channel estimation for the terahertz system," *IEEE J. Sel. Topics Signal Process.*, vol. 17, no. 4, pp. 878–892, 2023.
- [10] Y. Liu, C. Ouyang, Z. Wang, J. Xu, X. Mu, and A. L. Swindlehurst, "Near-field communications: A comprehensive survey," *IEEE Commun. Surveys Tuts*, 2024.
- [11] C. Ouyang, Y. Liu, X. Zhang, and L. Hanzo, "Near-field communications: A degree-of-freedom perspective," arXiv preprint arXiv:2308.00362, 2023.
- [12] R. Piestun and D. A. Miller, "Electromagnetic degrees of freedom of an optical system," *JOSA A*, vol. 17, no. 5, pp. 892–902, 2000.
- [13] H. Landau, "On szegő's eingenvalue distribution theorem and nonhermitian kernels," *Journal d'Analyse Mathématique*, vol. 28, no. 1, pp. 335–357, 1975.
- [14] H. J. Landau and H. Widom, "Eigenvalue distribution of time and frequency limiting," J. Math. Anal. Appl., vol. 77, no. 2, pp. 469–481, 1980
- [15] O. M. Bucci and G. Franceschetti, "On the degrees of freedom of scattered fields," *IEEE Trans. Antennas Propag.*, vol. 37, no. 7, pp. 918– 926, 1989.
- [16] M. Franceschetti, Wave theory of information. Cambridge University Press, 2017.
- [17] L. Ding, E. G. Ström, and J. Zhang, "Degrees of freedom in 3D linear large-scale antenna array communications—a spatial bandwidth approach," *IEEE J. Sel. Areas Commun.*, vol. 40, no. 10, pp. 2805– 2822, 2022.
- [18] L. Ding, J. Zhang, and E. G. Ström, "Spatial bandwidth asymptotic analysis for 3D large-scale antenna array communications," *IEEE Trans. Wireless Commun.*, vol. 23, no. 4, pp. 2638–2652, 2024.
- [19] A. Kosasih, Ö. T. Demir, N. Kolomvakis, and E. Björnson, "Spatial frequencies and degrees of freedom: Their roles in near-field communications," *IEEE Signal Process. Mag.*, vol. 42, no. 1, pp. 33–44, 2025.
- [20] Z. Wang, Y. Pan, J.-B. Wang, Y. Chen, and H. Yu, "Spatial bandwidth of bilateral near-field channels for linear large-scale antenna array system," in *Proc. Int. Conf. Wireless Commun. Signal Process. (WCSP)*. IEEE, 2024, pp. 348–353.
- [21] A. Tang, J.-B. Wang, Y. Pan, W. Zhang, X. Zhang, Y. Chen, H. Yu, and R. C. de Lamare, "Joint visibility region and channel estimation for extremely large-scale MIMO systems," *IEEE Trans. Commun.*, vol. 72, no. 10, pp. 6087–6101, 2024.
- [22] X. Shi, J. Wang, X. Wang, C. You, and J. Song, "Double-sided near-field XL-MIMO: Beamfocusing codeword selection and channel estimation," *IEEE Trans. Commun.*, vol. 73, no. 5, pp. 3441–3455, 2025.
- [23] Z. Wan, J. Zhu, and L. Dai, "Near-field channel modeling for electromagnetic information theory," arXiv preprint arXiv:2403.12268, 2024.
- [24] A. Tang, J.-B. Wang, Y. Pan, W. Zhang, Y. Chen, H. Yu, and R. C. De Lamare, "Line-of-sight extra-large MIMO systems with angular-domain processing: Channel representation and transceiver architecture," *IEEE Trans. Commun.*, vol. 72, no. 1, pp. 570–584, 2024.
- [25] Z. Wu, M. Cui, and L. Dai, "Enabling more users to benefit from near-field communications: From linear to circular array," *IEEE Trans. Wireless Commun.*, vol. 23, no. 4, pp. 3735–3748, 2024.
- [26] M. Franceschetti, M. D. Migliore, P. Minero, and F. Schettino, "The degrees of freedom of wireless networks via cut-set integrals," *IEEE Trans. Inf. Theory*, vol. 57, no. 5, pp. 3067–3079, 2011.
- [27] D. A. Miller, "Communicating with waves between volumes: evaluating orthogonal spatial channels and limits on coupling strengths," *Appl. Opt.*, vol. 39, no. 11, pp. 1681–1699, 2000.
- [28] H. Do, N. Lee, and A. Lozano, "Line-of-sight MIMO via intelligent reflecting surface," *IEEE Trans. Wireless Commun.*, vol. 22, no. 6, pp. 4215–4231, 2022.

- [29] K.-K. Wong, A. Shojaeifard, K.-F. Tong, and Y. Zhang, "Fluid antenna systems," *IEEE Trans. Wireless Commun.*, vol. 20, no. 3, pp. 1950–1962, 2021
- [30] L. Zhu, W. Ma, W. Mei, Y. Zeng, Q. Wu, B. Ning, Z. Xiao, X. Shao, J. Zhang, and R. Zhang, "A tutorial on movable antennas for wireless networks," *IEEE Commun. Surv. Tutorials.*, 2025.



Yijin Pan (Member, IEEE) received the B.S. and M.S. degree in communication engineering from Chongqing University in 2011 and 2014, respectively, and the Ph.D. degree from the School of Information Science and Engineering, Southeast University, Nanjing, China, in 2018. She was honored with the esteemed Royal Society Newton Fellowship in 2019. Currently, she serves as an Associate Professor at the School of Information Science and Engineering, Southeast University. She has been a TPC Member of IEEE ICC since 2015 and GLOBECOM

since 2017. Her research interests span the spectrum of wireless mobile communications, encompassing wireless signal processing, network resource and performance optimization, as well as embedded intelligent network terminal equipment.



Zhen Wang (Student Member, IEEE) received the B.S. degree from Nanjing University of Posts and Telecommunications, Nanjing, China, in 2023. He is currently pursuing the M.S. degree with the National Mobile Communications Research Laboratory, Southeast University, Nanjing, China. His research interests include extremely large-scale MIMO and reconfigurable intelligent surfaces (RIS).



Hongkang Yu received the B.E. degree from Beijing Jiaotong University, China, in 2016, and the Ph.D. degree from Peking University, China, in 2021. He is currently an Engineer with ZTE Corporation. His current research interests include mmWave, massive MIMO, and channel estimation.



Jiangzhou Wang (Fellow, IEEE) is a Professor at the Southeast University, China. His research interest is in mobile communications. He has published over 400 papers and 4 books. He was a recipient of the 2022 IEEE Communications Society Leonard G. Abraham Prize and IEEE Globecom 2012 best paper award. He was the Technical Program Chair of the 2019 IEEE International Conference on Communications (ICC2019), Shanghai, the Executive Chair of the IEEE ICC2015, London, and the Technical Program Chair of the IEEE WCNC2013. He is/was

an editor for a number of international journals, including IEEE Transactions on Communications from 1998 to 2013. Professor Wang is a Fellow of the Royal Academy of Engineering, U.K., Fellow of the IEEE, and Fellow of the IET.



Jun-Bo Wang (Senior Member, IEEE) received the B.S. degree in computer science from Hefei Univer sity of Technology, Hefei, China, in 2003, and the Ph.D. degree in communications engineering from Southeast University, Nanjing, China, in 2008. From October 2008 to August 2013, he was with Nanjing University of Aeronautics and Astronautics, China. From February 2011 to February 2013, he was a Post-Doctoral Fellow with the National Laboratory for Information Science and Technology, Tsinghua University, China. He is currently a Professor in the

National Mobile Communications Research Laboratory, Southeast University, Nanjing, China. From October 2016 to September 2018, he held the European Commission Marie Curie Fellowship and a Research Fellow with the University of Kent, U.K. His research interests include key technologies for future communication networks, especially for edge intelligence-enhanced communication schemes.



Kai-Kit Wong (M'01-SM'08-F'16) received the BEng, the MPhil, and the PhD degrees, all in Electrical and Electronic Engineering, from the Hong Kong University of Science and Technology, Hong Kong, in 1996, 1998, and 2001, respectively. After graduation, he took up academic and research positions at the University of Hong Kong, Lucent Technologies, Bell-Labs, Holmdel, the Smart Antennas Research Group of Stanford University, and the University of Hull, UK. He is Chair in Wireless Communications at the Department of Electronic and Electrical Engi-

neering, University College London, UK. His current research centers around 6G and beyond mobile communications. He is Fellow of IEEE and IET. He served as the Editor-in-Chief for IEEE Wireless Communications Letters between 2020 and 2023.



Yijian Chen received the B.S. degree from Central South University, Changsha, China, in 2006. He is currently a Senior Engineer of ZTE Corporation. His research interests include intelligent electromagnetic surface, electromagnetic information theory, holographic MIMO, and near-field communications.